Nanoscale

ROYAL SOCIETY OF CHEMISTRY

PAPER

View Article Online
View Journal | View Issue

Cite this: *Nanoscale*, 2020, **12**, 7986

Blending functionalised ligands to form multivariate metal–organic framework nanosheets (MTV-MONs) with tuneable surface chemistry†

David J. Ashworth and Jonathan A. Foster *

We report a new approach to tuning the properties of metal–organic framework nanosheets (MONs) by blending functionalised ligands to produce multivariate MONs (MTV-MONs). This approach enabled not only fine tuning of the MONs properties, but also resulted in MTV-MONs that show enhanced performance compared to their single-ligand counterparts. Layered copper paddle-wheel based MOFs were synthesised incorporating two or more 2,5-difunctionalised-benzene-1,4-dicarboxylate (fu-BDC) ligands. Liquid ultrasonic exfoliation resulted in the formation of nanosheets down to monolayer thickness presenting multiple functional moieties. Blending of ligands with relatively hydrophilic (methoxy-propoxy) and hydrophobic (pentoxy) moieties resulted in MTV-MONs that showed enhanced dispersion in both polar and apolar solvents compared to either single-ligand parent MON as well as intermediary binding properties. Blending of different fu-BDC ligands with different length alkoxy chains (methoxy-pentoxy) allowed incorporation of up to five different ligands within a single MTV-MON, including ligands which do not form this structure individually. This study demonstrates the potential of blending multiple ligands within an MTV-MON to enable fine-tuning of their structure and properties but also create new nanosheets which are more than the sum of their parts.

Received 5th February 2020,
Accepted 18th March 2020

DOI: 10.1039/d0nr01009j

rsc.li/nanoscale

1. Introduction

Two-dimensional (2D) materials have received considerable attention thanks to their high surface area, anisotropic structures and nanoscopic dimensions.[1–4] However, the simple inorganic composition of most of these materials means it is difficult to systematically alter the surface properties of these nanosheets without disrupting their structure or other properties.[5] For example, oxidation of hydrophobic graphene produces graphene oxide which is readily dispersible in water,[6] but this disrupts the conjugated backbone which gives rise to the remarkable electronic and mechanical properties of graphene. This process also leads to a range of different chemical functionalities (*e.g.* hydroxyl, aldehyde, carboxylic acid groups) being introduced to the surface at poorly defined positions in a way that is difficult to control systematically.[7] In some cases nanosheet properties can be tuned without disruption of the 2D structure through isoelectronic substitution of elements, such as in boron-doped graphitic carbon nitride,[8,9] or by doping structures with similarly sized ions, such as in perovskite[10,11] or MoS_2 nanosheets.[12,13] However, the limited pallet of elements available and subtle differences in substituted components limit the extent to which most nanosheets can be tuned in this way.

Metal–organic framework nanosheets (MONs) are nominally 2D, crystalline, free standing sheets formed of metal ion or cluster nodes which are linked in two dimensions with multitopic organic ligands.[14–23] Their diverse chemistry and 2D structure make them attractive candidates for a variety of sensing, catalysis,[24–26] separation,[27–30] composite materials[29,31] and electronics applications.[32–36] Moreover, in contrast to other 2D materials, the modular structure of MONs allows their structure and so properties to be systematically modified by using different organic linkers. A variety of isoreticular series of MONs have been developed in this way with modified linkers extending or reducing pore sizes or adding functional groups with different optical, electronic or chemical properties to the surface of MONs without fundamentally changing their structure.[37,38] The nanosheets have also been further modified through dative[39–42] or covalent[38] post-synthetic functionalisation to allow the introduction of new groups at well-defined positions on the MONs surface.

One strategy that has been extensively used to modify the properties of other molecular materials, but to our knowledge

Department of Chemistry, The University of Sheffield, Sheffield, UK, S3 7HF. E-mail: jona.foster@sheffield.ac.uk

† Electronic supplementary information (ESI) available: LC-MS, ^{1}H NMR, PXRD, Pawley refinement, FTIR, UV-Vis, binding studies, AFM, particle sizing. See DOI: 10.1039/d0nr01009j

has yet to be applied to MONs, is blending multiple different ligands non-stoichiometrically within a single framework. Terminology for this approach varies depending on field but co-polymers, solid-solutions and multicomponent gels[43–46] all share aspects of this approach. Most relevantly to this work, the concept of multivariate metal–organic frameworks (MTV-MOFs) was first developed by Yaghi and coworkers who combined up to eight different functionalised benzene-1,4-dicarboxylate (fu-BDC) ligands within a single phase of MOF-5-type structure in 2010.[47] Excitingly, MTV-MOFs have been shown to display enhanced properties compared to any of the single-ligand system they are composed of. For example, Yaghi and coworkers presented a tertiary blend of fu-BDC, where fu = NO_2, $(OC_3H_5)_2$ and $(OC_4H_7)_2$, which exhibited up to 400% better selectivity for CO_2 over CO compared with its best single-ligand counterpart.[47] Numerous authors have since utilised MTV-MOFs, mainly in regard to gas adsorption,[48] but also for creating "enzyme-like" pore spaces for selective catalysis.[49] The MTV-MOF concept has also been applied to incorporating multiple different metal-ions within a single framework,[50] for example within a M_3O metalated porphyrin-based MOF (M = Mg, Co, Ni and Fe).[51]

Blending multiple ligands within a single MON therefore has the potential to either: (1) allow for fine-tuning of the system's properties, intermediary to that of the single-ligand analogues or (2) combine properties of single-ligand analogues to create new phenomena not seen in either parent compound. However, the potential effects of blending ligands within MONs is distinct from those of MOFs where the focus is on controlling the internal structure of pores. Blending ligands with different functional groups has the potential to aid the exfoliation of layered MOFs to form MONs by weakening interlayer interactions and enhancing interaction with solvent molecules to aid dispersion. As MONs are dominated by their surface properties, the MTV-approach allows for fine-tuning of surface interactions important in sensing, catalysis, separation and composite materials applications.

We have previously presented isoreticular layered MOFs of the structure $[Cu(fu\text{-}BDC)(DMF)]_n$ using a number of different fu-BDC ligands: **1–5** and **5*** (Fig. 1).[52–54] These MOFs have the in-plane structure of MOF-2,[55,56] where dinuclear copper PW units are linked in two dimensions through dicarboxylate linkers and functional groups projecting between the layers. Through systematic studies we showed that the small changes in the length and polarity of the functional groups can have significant effect on the dimensions and concentration of the nanosheets formed.

Here, we synthesise a new series of layered MTV-MOFs using combinations of these linkers and exfoliate them to investigate the effect of different ligand combinations on the structure and properties of the resulting nanosheets. We hypothesised that blending of ligands with different properties could produce nanosheets with intermediate properties. We also speculated that random inclusion of the ligands[57] within the 2D net could reduce interlayer interactions and so lead to higher yields and thinner nanosheets than seen in any of the parent compounds.

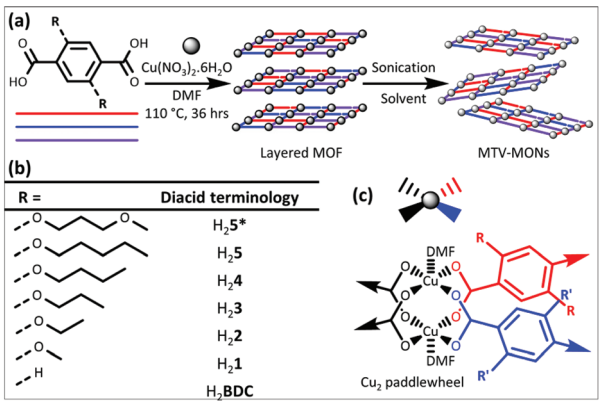

Fig. 1 (a) General schematic for the synthesis of multivariate Cu(fu-BDC)(DMF) based MONs, (b) nomenclature used for diacid ligand precursors and (c) copper paddle-wheel SBU.

2. Results and discussion

2.1. Blending hydrophilic and hydrophobic linkers

Previous studies have demonstrated the exfoliation of layered frameworks $[Cu(\mathbf{5}/\mathbf{5^*})(DMF)]_n$ to form MONs.[52–54] Incorporation of the 3-methoxypropoxy (**5***) or pentoxy (**5**) fu-BDC ligands imparted relatively hydrophilic or hydrophobic properties, respectively, to the MOF. Exfoliation in water or diethylether (Et_2O) produced higher concentrations of hydrophilic or hydrophobic MONs respectively, indicating that a good match of solvent and surface polarity may aid exfoliation. The surface chemistry in these systems is complicated by the potential of substitution or loss of co-ordinated solvent molecules at the axial position of the paddlewheels.[52] DFT modelling demonstrated H_2O could coordinate to the axial PW sites,[53] and Pawley and Rietveld refinement of high-resolution Synchrotron powder X-ray diffraction (PXRD) data enabled structural modelling of the frameworks both pre- and post-exfoliation in acetonitrile (MeCN).[54] MeCN was found to be a good solvent for exfoliation for these and other related Cu_2-PW based MOFs[38] and is used throughout this study unless otherwise stated.

A 50 : 50 mixture of H_2**5** and H_2**5*** diacids was used within a typical MOF synthesis. Copper nitrate trihydrate and diacids (totalling 110% of copper content, *i.e.* a 10% total ligand excess) were dissolved in DMF and sealed in a glass reaction vial with a Teflon-lined lid. This was heated to 110 °C for 36 h. The resulting microcrystalline MOF was washed and dried, yielding a blue microcrystalline powder. Further synthetic details can be found in the Experimental section. This general synthetic method was used for all MOF syntheses throughout this study.

Pawley refinement of the PXRD pattern indicated a structure with a unit cell very similar to that of the single-ligand MOFs (ESI Fig. S3 and Table S2†). This supports the formation of the anticipated layered structure of $[Cu(\mathbf{5^*})_{0.5}(\mathbf{5})_{0.5}(DMF)]_n$ (**5,5***-MTV-MOF). Approximately 2 mg of MOF was digested using 20 μL DCl (35%) in D_2O in 1 mL d_6-DMSO. Liquid

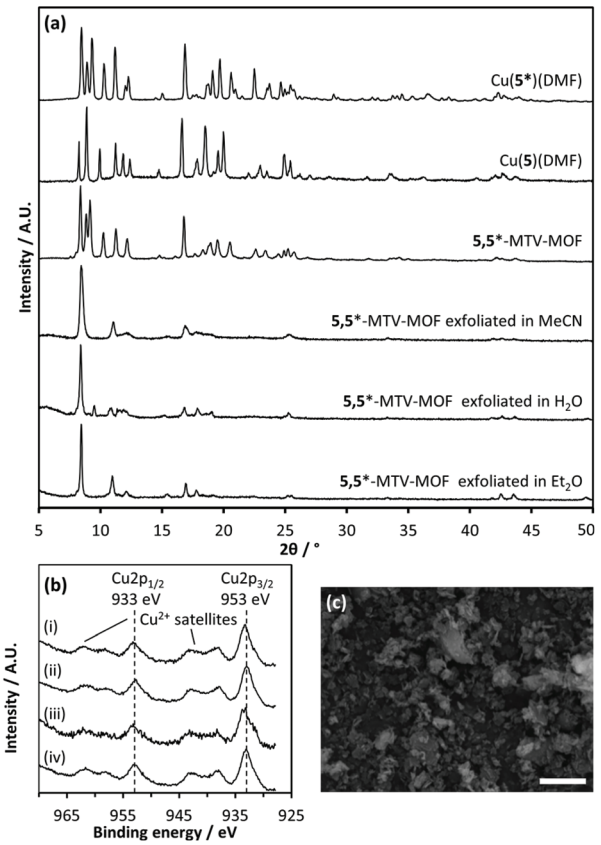

Fig. 2 (a) PXRD patterns of input MOF compared to single ligand MOFs,[53] and recollected material following exfoliation in MeCN, H_2O and Et_2O. (b) High-res XPS spectra of Cu 2p region of **5,5***-MTV-MOF (i), and then exfoliated in MeCN, H_2O and Et_2O (ii–iv, respectively). (c) SEM micrograph of **5,5***-MTV-MOF as-synthesised. Scale bar is 5 μm.

chromatography-mass spectrometry (LC-MS) confirmed the incorporation of both ligands within the MOF (m/z = 337.2 and 341.1 for $H5^-$ and $H5^{*-}$ respectively, ESI Fig. S1†). Proton-nuclear magnetic resonance (^{1}H NMR) was used to quantify the ligand content, using the α proton environments on the chains (found **5** = 53%, **5*** = 47%, ESI Fig. S2†). Elemental analysis was also consistent with the expected $[Cu(\mathbf{5})_{0.5}(\mathbf{5^*})_{0.5}(DMF)]_n$ ligand : DMF ratio for the fully solvated form (ESI Table S1†). Scanning electron microscopy (SEM) revealed plate-like particle morphology, with lateral dimensions of 0.5–5 μm, and apparent thicknesses of >100 nm (Fig. 2c).

5,5*-MTV-MOF was exfoliated in three different solvents: MeCN, H_2O and Et_2O. Solvent (2.4 mL) was added to a vial containing MOF powder (2 mg) and subjected to ultrasonication (12 h, 80 kHz) using our previously optimised protocol.[53] Centrifugation of the sonicated suspension (1 h, 1500 rpm) separated larger particles of unexfoliated material from the **5,5***-MTV-MONs which remained suspended in the supernatant, evidenced through Tyndall scattering. These sonication and centrifugation procedures are used throughout this manuscript.

To assess the structure of the materials produced, solids collected through centrifugation were air-dried and analysed using PXRD (Fig. 2a) and X-ray photoelectron spectroscopy (XPS, Fig. 2b). The XPS spectra were very similar across all samples, indicating the Cu(II) ions are in similar valence states post-exfoliation as in the MTV-MOF. Material exfoliated in all three solvents showed PXRD patterns with peaks which corresponded to those expected for the desolvated phase (loss of DMF from the axial position of the PW) as was reported for the parent single-ligand materials. Fourier-transform infrared spectroscopy (FTIR, ESI Fig. S14†) and ^{1}H NMR (ESI Fig. S11†) confirmed the absence of DMF in each case. Interestingly, exfoliation of **5,5***-MTV-MOFs in water produced the desolvated phase rather than the phase where water molecules replace DMF at the axial PW sites as observed in the single-ligand MOFs treated under the same conditions.[53] The MTV-MONs therefore show subtle differences in preferred structure compared to the parent MONs.

The concentration of the **5,5***-MTV-MON-containing supernatant was determined through UV-vis spectroscopy (ESI Fig. S15†). Calibration curves were previously prepared through titration of known MON concentration suspension into fresh solvent to calculate the extinction coefficients of the single-ligand parent MONs.[53] An average of these was taken for **5,5***-MTV-MON. This allowed calculation of unknown concentrations of suspension.

As shown in Table 1, single-ligand MONs were formed in high concentration in solvent that matches their surface chemistry and low concentration in the other, consistent with previous reports.[53] Interestingly, the **5,5***-MTV-MONs formed suspensions of higher concentration than that of either single-ligand MON in all three solvents. This is remarkable considering the MTV-MONs only possess approximately 50% of each surface functionality so might reasonably be expected to show intermediate preferences for solvent polarity. This therefore demonstrates the potential of combining multiple ligand functionalities to enhance the dispersion properties of MONs compared to either parent compound.

5,5*-MTV-MON suspensions were drop cast onto freshly cleaved mica substrates and were imaged using atomic force microscopy (AFM). SPIP software was used to size particles observed from exfoliation in MeCN (ESI Fig. S16†). Raw data from previous studies using single ligand MONs were re-sized using SPIP (ESI Fig. S22–26†). Average MON heights of 14 ±

Table 1 Concentrations of MONs in suspension after exfoliation in MeCN, water and diethyl ether, and binding constants for imidazole in water

	Concentration/mg mL^{-1}			
Input MOF	MeCN	H_2O	Et_2O	K_a/M^{-1}
5*-MOF	0.16	0.31	0.005	1950 ± 140[a]
5,5*-MTV-MOF	0.24	0.32	0.034	1640 ± 130
5-MOF	0.06	0.09	0.026	1370 ± 180[a]

[a] Data previously published in ref. 53.

10 nm were observed for **5,5***-MTV-MONs, with average lateral dimensions 280 ± 217 nm (n = 187). This is thinner than the average heights observed for the hydrophilic **5***-MONs (35 ± 18 nm) and similar to that of the hydrophobic **5**-MON (14 ± 8 nm), Dynamic light scattering (DLS) showed a number average diameter of 209 nm, compared to 213 nm and 179 nm for **5**- and **5***-MONs respectively.[53]

Exfoliation in H_2O yielded much larger MONs than in MeCN with lateral dimensions in the order of 400–5000 nm (although this was challenging to accurately size by this technique), with thicknesses >5 nm (Fig. 3a and ESI Fig. S17†). MONs appeared wrinkled and folded, indicating flexibility of these sheets.[58] SEM indicated lateral dimensions below 3 μm (Fig. 3b). Exfoliation in Et_2O yielded MONs of similar lateral ranges to MeCN, however ultrathin monolayer MONs were observed with thickness approximately 1.5 nm (Fig. 3c). Layer thickness is 1.4 nm according to crystal structures,[52,54] but this is calculated with chains fully extended, which is unlikely when at monolayer thickness. Large, ultrathin monolayer MONs such as these were not previously observed through exfoliation of single-ligand MOFs in Et_2O.

We previously showed that MONs can be used to sense model analytes and quantified their binding to the axial positions of the PWs.[53] Weak binding is observed in aqueous suspension due to competitive binding by water molecules with slightly stronger binding observed in the more hydrophobic system. DFT calculations indicate that the difference in binding strength is due to intramolecular co-ordination of the oxygen-lone pair to the axial position of the PW by the propoxy-methoxy chain.

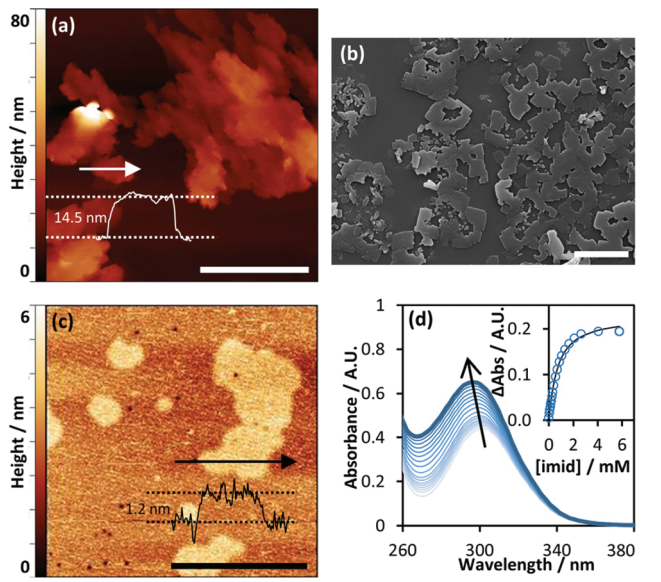

Fig. 3 AFM (a) and SEM (b) images of **5,5***-MTV-MOF exfoliated in water, and AFM image of **5,5***-MTV-MOF exfoliated in Et_2O (c), with height plots of the vectors indicated (a and c). Scale bars are 2, 5 and 2 μm, respectively. (d) UV-Vis titration showing addition of imidazole solution to an aqueous MON suspension; inset is a plot of ΔA against [imidazole], fitted to a binding curve.

5,5*-MTV-MONs were also investigated as sensors for imidazole in order to test whether ligands could be used to tune on binding strengths. An aqueous imidazole solution (20 mM) in MON suspension (0.18 mM) was titrated into an aqueous suspension of **5,5***-MTV-MONs (0.18 mM) and monitored using UV-Vis spectroscopy (Fig. 3d and ESI Fig. S19–21†). The binding constant was calculated from fitting Δ(absorbance) against [imidazole] as K_a = 1640 ± 130 M^{-1}, which is intermediary between that previously calculated for the single-ligand MONs (Table 1).[53] This demonstrates that MTV-MONs can have intermediary properties compared to single ligand parents.

2.2. Binary blending of different length alkyl chain functionalised ligands

We have previously reported an isoreticular series of layered MOFs using fu-BDC with propoxy-pentoxy alkoxy chains (ligands **3–5**).[54] We anticipated that there would be a tension between the linkers with longer chain lengths pushing the layers further apart and so weakening inter-layer interactions, and interdigitation of the chains increasing interlayer interactions and making shearing of the layers apart during exfoliation more difficult. Overall, our studies showed that the longer the alkoxy chain the thinner the nanosheets and wider their lateral dimensions. We hypothesised that blending longer and shorter alkyl chains might lead to even higher aspect ratio MONs with longer alkyl chains forcing the layers apart but shorter chains reducing interlayer interactions. We had previously also been unable to investigate the effect of shorter methoxy/ethoxy chain ligands (**1** and **2**), which did not form isoreticular layered structures, and therefore wondered if these ligands could be incorporated into MONs through blending with ligands that form the correct layered structure.

2.2.1. 3,5-MTV-MONs. Different ratios of H_2**3** and H_2**5** (where **3** and **5** correspond to the number of carbon atoms in the functional chains, see Fig. 1,) were mixed to form binary blends of **3,5**-MTV-MOFs with the target structure [Cu(**3**)$_x$(**5**)$_{1-x}$(DMF)]$_n$ (x = 0.10, 0.25, 0.50, 0.75 and 0.90). MOF syntheses proceeded as described above. ^{1}H NMR spectroscopy of digested samples indicated MTV-MOF ligand incorporation was broadly in-line with input, with the content of **3** calculated to be 0.14, 0.29, 0.52, 0.79 and 0.90, respectively (ESI Fig. S4†). Also evident from the ^{1}H NMR was that DMF content was not as predicted. In general, DMF content decreased with decreasing **5** fraction (ESI Table S3†).

PXRD of the **3,5**-MTV-MOFs showed that with a 0.9 fraction of **5**, the structure matched closely with that of [Cu(**5**)(DMF)]$_n$, however upon decreasing the **5** content and increasing the **3**, the PXRD patterns progressed from structure similar to [Cu(**5**)(DMF)]$_n$ to a structure similar to [Cu(**3**)]$_n$ (Fig. 4a). The structural transition could be due to irregular packing upon increasing **3** content within the microcrystals. As **3** is two methylene units shorter than **5**, there are fewer intralayer interactions between alkoxy chains and coordinated DMF molecules, which may favour the desolvated form upon increasing **3** content.

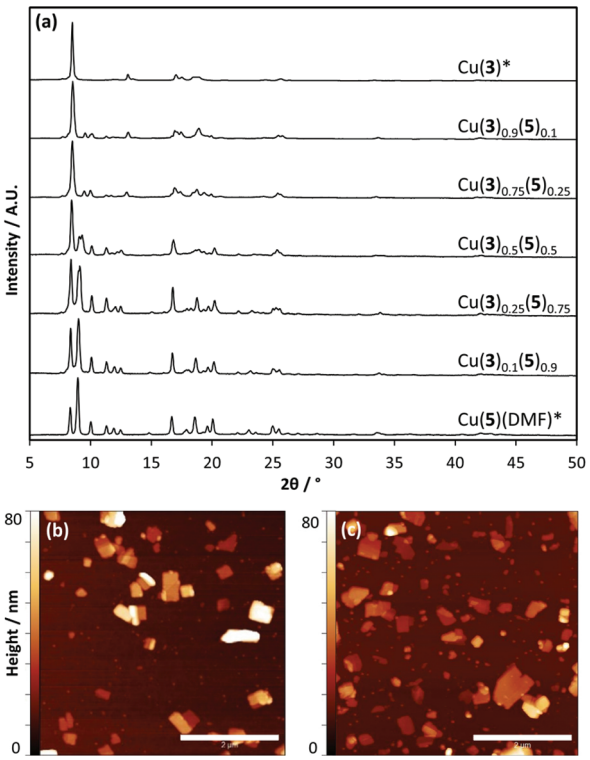

Fig. 4 (a) PXRD patterns of $Cu(3)_x(5)_{1-x}$ MTV-MOF, where x = 0.9, 0.75, 0.5, 0.25 and 0.1. (b and c) AFM topographic images of **3,5**-MTV-MONs resulting from exfoliation of **3,5**-MTV-MOFs in MeCN, where x = 0.5 and 0.1, respectively.

Liquid exfoliation of a subset of **3,5**-MTV-MOFs, where x = 0.9, 0.5 or 0.1, in MeCN yielded MON suspensions. AFM particle size analysis showed the lowest average height was for x = 0.1 (Fig. 4b, c, ESI Table S7 and ESI Fig. S27–29†), *i.e.* the largest fraction of 5–11 ± 6 nm (18 ± 10 and 16 ± 11 for x = 0.5 and 0.1 respectively). This fits with our previous study, where Cu(**5**) produced thinner MONs than Cu(**3**). Lateral dimensions for the three samples (x = 0.9, 0.5 and 0.1) were 281 ± 191, 333 ± 226 and 268 ± 198 nm, respectively.

2.2.2. 2,5-MTV-MONs. Layered MOF was synthesised using a 1 : 1 ratio of H_2**2**:H_2**5**. A slight excess of the ligand with shorter alkoxy chain **2** was again observed (0.67 fraction, ESI Table S4†). ^{1}H NMR analysis showed negligible DMF content (Fig. S6†) and PXRD indicated a structure similar to the desolvated phase that was observed for high fractions of **3** in **3,5**-MTV-MOFs (ESI Fig. S5†).

AFM of **2,5**-MTV-MONs following exfoliation in MeCN revealed notably angular MONs with edges up to 450 nm long. Heights ranged up to 70 nm, with a few elongated oblong particles observed up to 250 nm. Particle sizing showed an average length of 315 ± 133 nm and height of 33 ± 17 nm (ESI Fig. S32†).

2.2.3. 2,3-MTV-MONs. MOF synthesis using a 1 : 1 ratio of H_2**2** and H_2**3** showed near quantitative ligand inclusion (0.51 : 0.49). PXRD indicated a phase similar to that of [Cu(**3**)(DMF)]$_n$ (Fig. S5†), however there are some additional diffraction peaks which cannot be accounted for from this structure. This could be indicative of the presence of a secondary phase. ^{1}H NMR indicated a relative DMF content of 0.54 (Fig. S6†), which suggests a possible identity of the secondary phase as the desolvated structure. However, diffraction peaks could also relate to an unknown form with **2**-containing MOF. High resolution Synchrotron diffraction data could be collected to inform more on the structure of these materials.

Particle sizing of **2,3**-MTV-MONs exfoliated in MeCN showed an average length of 196 ± 87 nm and particle height of 12 ± 6 nm (ESI Fig. S31†). This is both the thinnest average height and narrowest distribution observed thus far for these materials (see Fig. 5c). The inclusion of shorter-chain **2** within this MTV framework may aid exfoliation compared to just [Cu(**3**)(DMF)]$_n$, due to reduced interdigitation of chains between layers, resulting in decreased interlayer interactions.

2.3. Higher order blends of alkyl chain functionalised ligands

In order to explore the extent to which this MTV concept can be pushed within these layered frameworks, combinations of up to five different ligands (**1**–**5**) were blended within MOF syntheses. The ratios of different ligands and the DMF content were quantified through ^{1}H NMR (Fig. 5b and ESI Fig. S9–10†) and are summarised in ESI Table S5.† The α-proton environments of the alkoxy chains were used to assign blends incorporating **1** or **2**, as the chemical shift for each ligands' α-protons was similar (chemical shift ranging from 3.76 (**1**) to 4.01 (**2**). The ratio of ligand found to be included within the MOFs was broadly consistent with the input reagent ratios in all cases. Contrary to the binary blends, this suggests that the synthetic kinetics are similar for each ligand, which may be a result of more random. Local combinations of ligands not exhibiting as much steric pressure PXRD of the MTV-MOFs indicated that with the increasing number of ligands incorporated, the MOFs adopt a structure similar to that of the desolvated single-ligand MOF structure of [Cu(**3**–**5**)]$_n$ (see Fig. 5a). This is corroborated by the decreased DMF content of the materials (ESI Table S5†). The fact that there was still some DMF observed by 1H NMR may result from DMF that remained in the pore spaces created by inefficient packing between different length alkoxy chains between layers of the MTV-framework. PXRD of solids collected through centrifugation post-exfoliation in MeCN indicated that the desolvated structure had been maintained (Fig. 5a), and that this structure was similar across each MTV material, consistent with the desolvated structure of the single-ligand parent materials.[54]

It is worth noting that ligands **1** and **2** were successfully incorporated within these MTV frameworks. Single ligand MOF syntheses using these ligands did not result in the desired layered structure. Incorporation of these within blended systems may facilitate their inclusion within the framework. MTV-MOFs therefore provide a route to adding non-layer forming ligands, offering opportunities for more advanced 2D layer framework design.

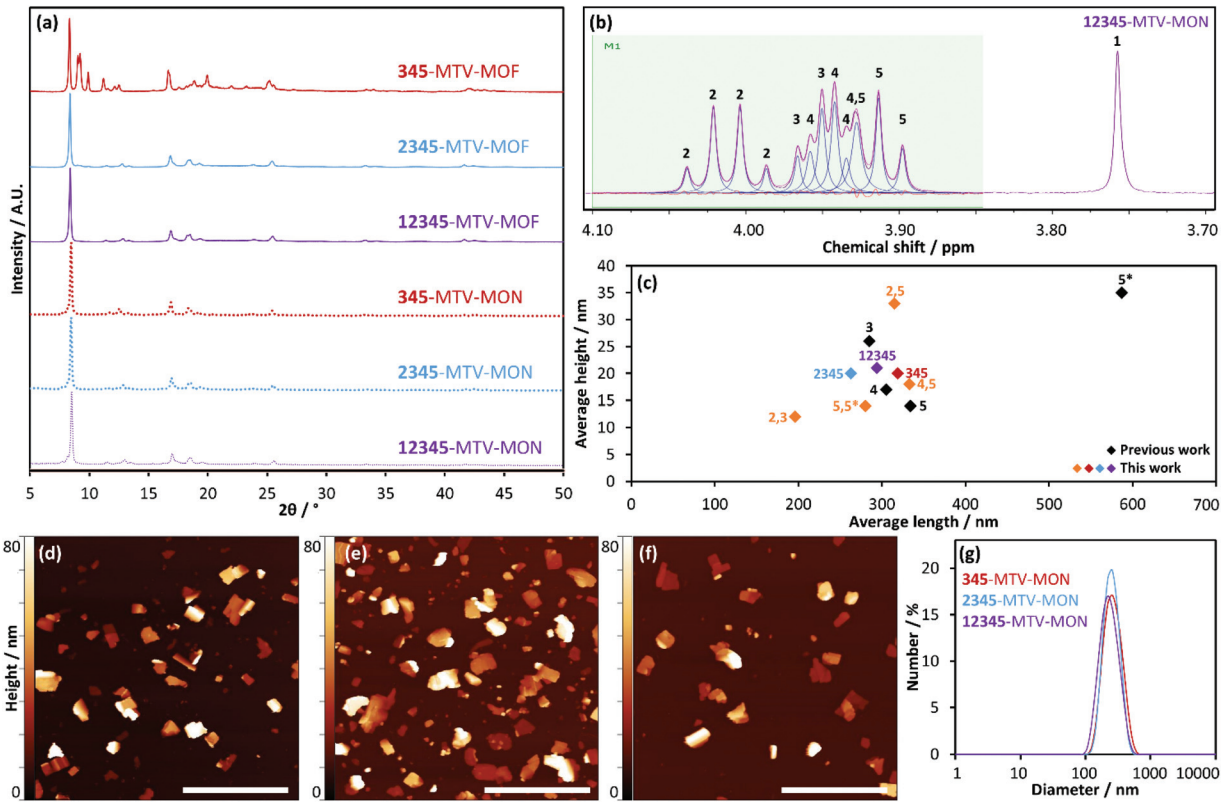

Fig. 5 (a) PXRD patterns of MTV-MOFs as synthesised (solid lines), and material recollected from centrifugation following ultrasonic exfoliation in MeCN (MTV-MONs, dotted lines). (b) Example deconvolution of the α-proton region for diacids H_2**1**–**5** from a digested sample of **12345**-MTV-MON. Alkoxy proton contributions from the different diacids are indicated. Spectral trace is purple, deconvoluted peaks are blue, the fitted line is pink and the difference plot is red. (c) Average particle size data determined using SPIP software. Black diamonds are from reanalysed MON images from references 53 and 54, coloured diamonds are new MTV-MONs presented in this work. (d–f) AFM topographical images of **345**-, **2345**- and **12345**-MTV-MONs, respectively, from exfoliation in MeCN. Lateral scale bars are 2 μm. (g) DLS data for MTV-MONs in MeCN.

Average particle heights and lateral dimensions of the MTV-MONs measured by AFM (Fig. 5d–f and ESI Fig. S34–36†) are summarised in Table 2. Notably, the average heights, around 20 ± 11 nm, and distributions (ESI Fig. S37†) of the tertiary-quinternary blends are remarkably similar. The average lengths observed by AFM range between 263–219 nm (broadly matching those observed by DLS, Fig. 5g) but sit within a broad particle size distribution meaning no significant trends are observed. This indicates that no further improvements in the aspect ratio of this series of MTV-MONs is achieved by using higher order blends of mismatched ligands.

Table 2 Summary of MON particle size data

MON	*n*	Length	Height	AR[a]	Diam.[b]
3	150	285 ± 151	26 ± 17	15 ± 10	185[c]
4	113	305 ± 162	17 ± 10	20 ± 10	213[c]
5	115	334 ± 195	14 ± 8	26 ± 13	247[c]
5*	61	587 ± 262	35 ± 18	18 ± 4	179[d]
5,5*-MTV-MON	187	280 ± 217	14 ± 10	29 ± 29	210
3,5-MTV-MON	62	333 ± 223	18 ± 10	20 ± 12	221
2,5-MTV-MON	55	315 ± 133	33 ± 17	11 ± 6	197
3,5-MTV-MON	70	196 ± 87	12 ± 6	18 ± 8	109
345-MTV-MON	90	319 ± 204	20 ± 11	18 ± 10	214
2345-MTV-MON	173	263 ± 201	20 ± 10	14 ± 10	215
12345-MTV-MON	53	294 ± 148	21 ± 12	18 ± 12	186

All size values are in nm. [a] AR = aspect ratio, defined as length/height (calculated for each particle). [b] Hydrodynamic diameter according to number average DLS data. [c] Data reproduced with permission from ref. 54. [d] Data reproduced with permission from ref. 35.

3. Conclusions

In this study we introduce MTV-MONs as a new approach to tuning the properties of MONs. An isoreticular series of layered MTV-MOFs based on the Cu-PW motif were formed using combinations of six different benzene-1,4-dicarboxylic acid linkers (**1**–**5**, **5***) functionalised with alkoxy chains of different polarities and lengths. Ultrasonic liquid exfoliation of the MOFs produced suspensions of MONs in different solvents, with examples observed down to monolayer thickness. We have demonstrated the ability of MTV-MONs to act as sensors for imidazole from aqueous suspension. The binding constant for imidazole to the axial position off 1 : 1 **5,5***-MTV-MONs was found to be intermediate compared to those of the parent single-ligand nanosheets, demonstrating that blending ligands can allow for fine-tuning of properties. In

addition, these MTV-MONs counterintuitively formed higher concentrations of thinner nanosheets in both diethyl ether and water compared to either of the parent compounds, illustrating that MTV-MONs can exhibit enhanced behaviour compared to single-ligand parent compounds.

Blends of BDC functionalised with different alkyl chains resulted in MTV-MOFs of up to quinternary composition, which shared a common structure. We had hypothesised that increasing mismatch in chain length would aid exfoliation, however this was not observed. **2,3**-MTV-MONs produced the thinnest nanosheets on average whilst those with the largest mis-match in chain length, **2,5**-MTV-MONs, produced the thickest nanosheets, although these are relatively subtle effects within broad particle size distributions. The inclusion of ligands **1** and **2** into MTV structures demonstrates how the MTV-approach can be used to include ligands and their functionalities which would not form nanosheets by themselves.

As with MOFs, we anticipate the MTV approach will be broadly applicable across a wide variety of different MON architectures and will provide a route to fine-tuning of their sensing, catalytic, separation and electronic properties.[59–62] The approach also offers distinct new opportunities to address challenges specific to MON formation, such as tuning interlayer interactions to enhance exfoliation and surface properties to stabilise the nanosheets in suspension. Most excitingly, blending multiple different functional groups in this way can lead to synergistic effects that result in new materials which are more than the sum of their parts.

4. Experimental

4.1. Materials

Materials were purchased from commercial suppliers and used without further purification.

4.2. fu-H_2BDC ligand precursor syntheses

fu-H_2BDC derivatives H_2(**1–5,5***) were prepared according to previously demonstrated methods.[52–54,63] Briefly, the fu-H_2BDC was synthesised through Williamson etherification of protected dimethyl-2,5-dihydroxybenzene-1,4-dicarboxylic acid with the corresponding fu-halide (bromide in all cases except iodide for H_2**1**). Deprotection in base and subsequent work-up in acid yielded the desired fu-H_2BDC diacid in high yields of 77–91%.

4.3. MOF syntheses

All MOFs were synthesised on a 20–30 mg scale using a common method with mole calculations based on the anticipated structural formula $[Cu(fu\text{-}BDC)(DMF)]_n$ using a total 10% excess of ligands.[54] For example, the synthesis of 20 mg **5,5***-MTV-MOF – $[Cu(\mathbf{5,5^*})(DMF)]_n$ – requires 0.42 mmol copper ($CuC_{20}H_{29}NO_8$, Mr = 475.00 Da). Copper nitrate trihydrate (0.42 mmol) and diacid ligand precursors H_2**5** (0.23 mmol) and H_2**5*** (0.23 mmol) were dissolved in DMF (6 mL) and sealed into a 20 mL glass reaction vial sealed with a Teflon-lined lid. This was heated at 10 C min^{-1} to 110 °C, held for 36 h, then cooled at 0.1 °C min^{-1} to 25 °C. The vial contents were transferred to a centrifuge tube and washed through centrifugation with DMF (3 × 5 mL) and Et_2O (3 × 5 mL), then transferred to a clean vial and air-dried at room temperature, yielding a blue microcrystalline powder of $[Cu(\mathbf{5})_{0.53}(\mathbf{5^*})_{0.47}(DMF)]_n$ (18.1 mg, 91%). All MOF syntheses used this general synthetic method, using a total ligand excess of 10%. For 30 mg target MOF syntheses, 9 mL DMF was used instead of 6 mL.

4.4. Liquid ultrasonic exfoliation

2 mg of MOF was suspended in 2.4 mL solvent (MeCN, water or Et_2O) and vortexed for 30 s then sonicated for 12 h using a Fisher brand Elmasonic P 30H ultrasonic bath operating at 80 kHz and 100% power (320 W). Samples were rotated using an overhead stirrer to ensure even exposure and the bath was fitted with a water coil to maintain temperature at approximately 18–21 °C.[53] After sonication, samples were transferred to a centrifuge tube and centrifuged for 1 h at 1500 rpm, which recollected unexfoliated material and yielded MON-containing supernatant.

4.5. Characterisation

Room temperature ^{1}H NMR spectroscopy was performed with a Bruker Avance IIIHD 400 MHz spectrometer. ^{1}H chemical shifts are reported in parts per million on the δ scale and referenced to the residual proton resonance of the solvent. Approximately 2 mg MOF was digested using 20 μL DCl (35%) in D_2O and 1 mL d_6-DMSO, resulting in solutions of diacid ligand precursors for quantification. LC-MS data were collected using an Agilent 6530 QTOF LC-MS operating in negative mode electrospray ionisation, using the samples prepared for ^{1}H NMR. PXRD were recorded using a Bruker D8 Advance powder X-ray diffractometer equipped with a Lynxeye detector, using Cu K_α radiation (λ = 1.5406 Å) operating in capillary mode (MOFs) or flat-plate mode (materials recollected from centrifugation. For capillary mode, samples were ground and loaded into a 0.7 mm internal diameter borosilicate capillary. For flat plate, samples were sprinkled onto a low-background silicon plate. XPS was carried out using a Kratos Ultra instrument with a monochromated Al source. Powder samples were mounted onto the sample holder by lightly pressing them into indium foil. Charge neutralisation was used. Survey scans were collected between 1200 to 0 eV binding energy, at 160 eV pass energy and 1 eV intervals. High-resolution O 1s, C 1s, Cu 2p and Cu LMM spectra were collected over an appropriate energy range at 20 eV pass energy and 0.1 eV intervals. FTIR spectra were recorded with a PerkinElmer Spectrum One spectrometer equipped with a diamond ATR accessory. Data were collected from 500 to 4000 cm^{-1} using a resolution of 1 cm^{-1} and 8 scans. Elemental analysis was performed with an Elementar vario MICRO cube. UV-Vis spectroscopy was performed on a Cary 50 UV-Vis spectrophotometer, in the range 800–200 nm (solvent dependant) with a 1 nm resolution and 600 nm min^{-1} scan speed. Samples were prepared for SEM analysis on a

carbon sticky tab loaded on an aluminium sample stub and coated with approximately 20 nm gold using an Edwards S150B sputter coater. SEM micrographs were collected using a TESCAN VEGA3 LMU SEM instrument operating in secondary electron mode. AFM was performed with a Bruker Multimode 5 AFM operating in soft-tapping mode using Bruker OTESPA-R3 cantilevers. Samples were prepared by drop-casting 10 μL MON suspension onto freshly cleaved mica held on a magnetic sample holder which was pre-heated to just below the boiling point of the solvent. Images were processed using standard techniques within Gwyddion image processing software.[64] DLS data were collected using a Malvern Zetasizer Nano Series particle size analyzer equipped with a He–Ne laser at 633 nm, operating in backscatter mode (173°).

4.6. Particle sizing

Particle sizing was performed using SPIP software. Prior to analysis, AFM images were plane levelled, scars were removed and the background was zeroed. The particle and pore analysis tool was used to pick and size particles. The "threshold" detection method was used, which varied between images depending on how well the background had been levelled, between 3 and 9 nm. Post-processing filters for particle inclusion were used across all images: (i) minimum length of 80 nm to neglect image defects and small fragments on the sample surface; (ii) minimum height of 6 nm to avoid detecting small errors in the scan; (iii) maximum height of 150 nm to neglect large particles/agglomerates or jumps in the probe/surface contact. Particles that lay partly on an edge of the image were not included.

Conflicts of interest

There are no conflicts to declare.

Acknowledgements

This work was performed at The University of Sheffield. D. J. A. and J. A. F. thank the EPSRC (EP/K503149/1 and EP/R513313/1), the Ramsay Memorial Fellowship (JAF), the University of Sheffield's Vice Chancellors Fellowship (JAF) and the Royal Society (RG170002) for funding. With thanks to Michael Harris, Chris Hill and the University of Sheffield BioMedical Sciences EM unit for SEM analyses, and Dr Deborah Hammond and the Sheffield Surface Analysis Centre for XPS analyses.

Notes and references

1 G. R. Bhimanapati, Z. Lin, V. Meunier, Y. Jung, J. Cha, S. Das, D. Xiao, Y. Son, M. S. Strano, V. R. Cooper, L. Liang, S. G. Louie, E. Ringe, W. Zhou, S. S. Kim, R. R. Naik, B. G. Sumpter, H. Terrones, F. Xia, Y. Wang, J. Zhu, D. Akinwande, N. Alem, J. A. Schuller, R. E. Schaak, M. Terrones and J. A. Robinson, *ACS Nano*, 2015, **9**, 11509–11539.
2 F. Wang, Z. Wang, L. Yin, R. Cheng, J. Wang, Y. Wen, T. A. Shifa, F. Wang, Y. Zhang, X. Zhan and J. He, *Chem. Soc. Rev.*, 2018, **47**, 6296–6341.
3 C. Anichini, W. Czepa, D. Pakulski, A. Aliprandi, A. Ciesielski and P. Samorì, *Chem. Soc. Rev.*, 2018, **47**, 4860–4908.
4 G. Bottari, M. Ángeles Herranz, L. Wibmer, M. Volland, L. Rodríguez-Pérez, D. M. Guldi, A. Hirsch, N. Martín, F. D'Souza and T. Torres, *Chem. Soc. Rev.*, 2017, **46**, 4464–4500.
5 R. Mas-Ballesté, C. Gómez-Navarro, J. Gómez-Herrero and F. Zamora, *Nanoscale*, 2011, **3**, 20–30.
6 S. Abdolhosseinzadeh, H. Asgharzadeh and H. S. Kim, *Sci. Rep.*, 2015, **5**, 10160.
7 W. Gao, L. B. Alemany, L. Ci and P. M. Ajayan, *Nat. Chem.*, 2009, **1**, 403–408.
8 X. Wang, G. Sun, P. Routh, D. H. Kim, W. Huang and P. Chen, *Chem. Soc. Rev.*, 2014, **43**, 7067–7098.
9 S. Thaweesak, S. Wang, M. Lyu, M. Xiao, P. Peerakiatkhajohn and L. Wang, *Dalton Trans.*, 2017, **46**, 10714–10720.
10 P. Xu, T. J. Milstein and T. E. Mallouk, *ACS Appl. Mater. Interfaces*, 2016, **8**, 11539–11547.
11 J. Wang, J. Dong, F. Lu, C. Sun, Q. Zhang and N. Wang, *J. Mater. Chem. A*, 2019, **7**, 23563–23576.
12 R. Li, L. Yang, T. Xiong, Y. Wu, L. Cao, D. Yuan and W. Zhou, *J. Power Sources*, 2017, **356**, 133–139.
13 X. Dai, K. Du, Z. Li, M. Liu, Y. Ma, H. Sun, X. Zhang and Y. Yang, *ACS Appl. Mater. Interfaces*, 2015, **7**, 27242–27253.
14 D. Rodríguez-San-Miguel, P. Amo-Ochoa and F. Zamora, *Chem. Commun.*, 2016, **52**, 4113–4127.
15 R. Sakamoto, K. Takada, T. Pal, H. Maeda, T. Kambe and H. Nishihara, *Chem. Commun.*, 2017, **53**, 5781–5801.
16 W. Zhao, J. Peng, W. Wang, S. Liu, Q. Zhao and W. Huang, *Coord. Chem. Rev.*, 2018, **377**, 44–63.
17 M. Zhao, Y. Huang, Y. Peng, Z. Huang, Q. Ma and H. Zhang, *Chem. Soc. Rev.*, 2018, **47**, 6267–6295.
18 M. Xu, S. S. Yang and Z.-Y. Gu, *Chem. – Eur. J.*, 2018, **24**, 15131–15142.
19 D. J. Ashworth and J. A. Foster, *J. Mater. Chem. A*, 2018, **6**, 16292–16307.
20 J. Duan, Y. Li, Y. Pan, N. Behera and W. Jin, *Coord. Chem. Rev.*, 2019, **395**, 25–45.
21 A. Dhakshinamoorthy, A. M. Asiri and H. Garcia, *Adv. Mater.*, 2019, **31**, 1900617.
22 S. Kim, H. Wang and Y. M. Lee, *Angew. Chem., Int. Ed.*, 2019, **58**, 17512–17527.
23 Y. Peng and W. Yang, *Sci. China: Chem.*, 2019, **62**, 1561–1575.
24 G. Zhan and H. C. Zeng, *Adv. Funct. Mater.*, 2016, **26**, 3268–3281.
25 Y. Huang, M. Zhao, S. Han, Z. Lai, J. Yang, C. Tan, Q. Ma, Q. Lu, J. Chen, X. Zhang, Z. Zhang, B. Li, B. Chen, Y. Zong and H. Zhang, *Adv. Mater.*, 2017, **29**, 1700102.

26 J. Huang, Y. Li, R. K. Huang, C. T. He, L. Gong, Q. Hu, L. Wang, Y. T. Xu, X. Y. Tian, S. Y. Liu, Z. M. Ye, F. Wang, D. D. Zhou, W. X. Zhang and J. P. Zhang, *Angew. Chem., Int. Ed.*, 2018, **57**, 4632–4636.
27 Y. Peng, Y. Li, Y. Ban, H. Jin, W. Jiao, X. Liu and W. Yang, *Science*, 2014, **346**, 1356–1359.
28 Y. Peng, Y. Li, Y. Ban and W. Yang, *Angew. Chem., Int. Ed.*, 2017, **56**, 9757–9761.
29 S. Feng, M. Bu, J. Pang, W. Fan, L. Fan, H. Zhao, G. Yang, H. Guo, G. Kong, H. Sun, Z. Kang and D. Sun, *J. Membr. Sci.*, 2020, **593**, 117404.
30 Z.-R. Tao, J.-X. Wu, Y.-J. Zhao, M. Xu, W.-Q. Tang, Q.-H. Zhang, L. Gu, D.-H. Liu and Z.-Y. Gu, *Nat. Commun.*, 2019, **10**, 2911.
31 Z. Bai, S. Liu, G. Cheng, G. Wu and Y. Liu, *Microporous Mesoporous Mater.*, 2020, **292**, 109763.
32 D. Sheberla, L. Sun, M. A. Blood-Forsythe, S. Er, C. R. Wade, C. K. Brozek, A. Aspuru-Guzik and M. Dincă, *J. Am. Chem. Soc.*, 2014, **136**, 8859–8862.
33 K. Takada, R. Sakamoto, S. T. Yi, S. Katagiri, T. Kambe and H. Nishihara, *J. Am. Chem. Soc.*, 2015, **137**, 4681–4689.
34 C. Li, X. Hu, W. Tong, W. Yan, X. Lou, M. Shen and B. Hu, *ACS Appl. Mater. Interfaces*, 2017, **9**, 29829–29838.
35 J.-X. Wu, S.-Z. Hou, X.-D. Zhang, M. Xu, H.-F. Yang, P.-S. Cao and Z.-Y. Gu, *Chem. Sci.*, 2019, **10**, 2199–2205.
36 C. Hermosa, B. R. Horrocks, J. I. Martínez, F. Liscio, J. Gómez-Herrero and F. Zamora, *Chem. Sci.*, 2015, **6**, 2553–2558.
37 G. Lan, Y. Quan, M. Wang, G. T. Nash, E. You, Y. Song, S. S. Veroneau, X. Jiang and W. Lin, *J. Am. Chem. Soc.*, 2019, **141**, 15767–15772.
38 J. Nicks, J. Zhang and J. A. Foster, *Chem. Commun.*, 2019, **55**, 8788–8791.
39 Z. Lin, N. C. Thacker, T. Sawano, T. Drake, P. Ji, G. Lan, L. Cao, S. Liu, C. Wang and W. Lin, *Chem. Sci.*, 2017, **9**, 143–151.
40 R. Xu, Z. Cai, G. Lan and W. Lin, *Inorg. Chem.*, 2018, **57**, 10489–10493.
41 G. Lan, Z. Li, S. S. Veroneau, Y.-Y. Zhu, Z. Xu, C. Wang and W. Lin, *J. Am. Chem. Soc.*, 2018, **140**, 12369–12373.
42 G. Lan, Y. Quan, M. Wang, T. Nash, E. You, Y. Song, S. S. Veroneau, X. Jiang and W. Lin, *J. Am. Chem. Soc.*, 2019, **141**, 15767–15772.
43 L. E. Buerkle and S. J. Rowan, *Chem. Soc. Rev.*, 2012, **41**, 6089–6102.
44 J. A. Foster, R. M. Edkins, G. J. Cameron, N. Colgin, K. Fucke, S. Ridgeway, A. G. Crawford, T. B. Marder, A. Beeby, S. L. Cobb and J. W. Steed, *Chem. – Eur. J.*, 2014, **20**, 279–291.
45 R. Muthuraj and T. Mekonnen, *Polymer*, 2018, **145**, 348–373.
46 M. Lusi, *Cryst. Growth Des.*, 2018, **18**, 3704–3712.
47 H. Deng, C. J. Doonan, H. Furukawa, R. B. Ferreira, J. Towne, C. B. Knobler, B. Wang and O. M. Yaghi, *Science*, 2010, **327**, 846–850.
48 A. Helal, Z. H. Yamani, K. E. Cordova and O. M. Yaghi, *Natl. Sci. Rev.*, 2017, **4**, 296–298.
49 A. M. Fracaroli, P. Siman, D. A. Nagib, M. Suzuki, H. Furukawa, F. D. Toste and O. M. Yaghi, *J. Am. Chem. Soc.*, 2016, **138**, 8352–8355.
50 B. Tu, Q. Pang, E. Ning, W. Yan, Y. Qi, D. Wu and Q. Li, *J. Am. Chem. Soc.*, 2015, **137**, 13456–13459.
51 Q. Liu, H. Cong and H. Deng, *J. Am. Chem. Soc.*, 2016, **138**, 13822–13825.
52 J. A. Foster, S. Henke, A. Schneemann, R. A. Fischer and A. K. Cheetham, *Chem. Commun.*, 2016, **52**, 10474–10477.
53 D. J. Ashworth, A. Cooper, M. Trueman, R. W. M. Al-Saedi, S. D. Liam, A. J. Meijer and J. A. Foster, *Chem. – Eur. J.*, 2018, **24**, 17986–17996.
54 D. J. Ashworth, T. M. Roseveare, A. Schneemann, M. Flint, I. Dominguez Bernáldes, P. Vervoorts, R. A. Fischer, L. Brammer and J. A. Foster, *Inorg. Chem.*, 2019, **58**, 10837–10845.
55 H. Li, M. Eddaoudi, T. L. Groy and O. M. Yaghi, *J. Am. Chem. Soc.*, 1998, **120**, 8571–8572.
56 C. G. Carson, K. Hardcastle, J. Schwartz, X. Liu, C. Hoffmann, R. A. Gerhardt and R. Tannenbaum, *Eur. J. Inorg. Chem.*, 2009, **16**, 2338–2343.
57 X. Kong, H. Deng, F. Yan, J. Kim, J. A. Swisher, B. Smit, O. M. Yaghi and J. A. Reimer, *Science*, 2013, **341**, 882–885.
58 W. Bai, S. Li, J. Ma, W. Cao and J. Zheng, *J. Mater. Chem. A*, 2019, **7**, 9086–9098.
59 J. López-Cabrelles, S. Mañas-Valero, I. J. Vitórica-Yrezábal, P. J. Bereciartua, J. A. Rodríguez-Velamazán, J. C. Waerenborgh, B. J. C. Vieira, D. Davidovikj, P. G. Steeneken, H. S. J. van der Zant, G. Mínguez Espallargas and E. Coronado, *Nat. Chem.*, 2018, **10**, 1001–1007.
60 M. J. Cliffe, E. Castillo-Martínez, Y. Wu, J. Lee, A. C. Forse, F. C. N. Firth, P. Z. Moghadam, D. Fairen-Jimenez, M. W. Gaultois, J. A. Hill, O. V. Magdysyuk, B. Slater, A. L. Goodwin and C. P. Grey, *J. Am. Chem. Soc.*, 2017, **139**, 5397–5404.
61 G. Lan, K. Ni, R. Xu, K. Lu, Z. Lin, C. Chan and W. Lin, *Angew. Chem., Int. Ed.*, 2017, **56**, 12102–12106.
62 Y. Guo, W. Shi, H. Yang, Q. He, Z. Zeng, J. Y. Ye, X. He, R. Huang, C. Wang and W. Lin, *J. Am. Chem. Soc.*, 2019, **141**, 17875–17883.
63 J. M. Chem, S. Henke, A. Schneemann, S. Kapoor, R. A. Fischer, R. Winter and R. A. Fischer, *J. Mater. Chem.*, 2012, **22**, 909–918.
64 D. Nečas and P. Klapetek, *Cent. Eur. J. Phys.*, 2012, **10**, 181–188.